



Evolution of the Coronal Cavity From the Quiescent to Eruptive Phase Associated with Coronal Mass Ejection

Ranadeep Sarkar¹ , Nandita Srivastava¹ , Marilena Mierla^{2,3} , Matthew J West² , and Elke D’Huys²

¹ Udaipur Solar Observatory, Physical Research Laboratory, Badi Road, Udaipur 313001, India; ranadeep@prl.res.in

² Solar-Terrestrial Center of Excellence—SIDC, Royal Observatory of Belgium, 1180 Brussels, Belgium

³ Institute of Geodynamics of the Romanian Academy, Bucharest, Romania

Received 2018 December 25; revised 2019 March 14; accepted 2019 March 19; published 2019 April 22

Abstract

We present the evolution of a coronal cavity encompassing its quiescent and eruptive phases in the lower corona. Using multiple vantage-point observations from the *SDO/AIA*, *STEREO SECCHI/EUVI*, and *PROBA2/Sun Watcher* with the APS and Image Processing (SWAP) extreme ultraviolet (EUV) imagers, we capture a sequence of quasi-static equilibria of the quiescent cavity, which exhibited a slow rise and an expansion phase during its passage on the solar disk from 2010 May 30 to June 13. By comparing the decay-index profiles of the cavity system during the different stages of its quiescent and pre-eruptive phases, we find that the decay-index value at the cavity centroid height can be used as a good indicator to predict the cavity eruption in the context of torus instability. Combining the observations of SWAP and the Large Angle and Spectrometric Coronagraph Experiment C2/C3, we show the evolution of the EUV cavity into the white-light cavity as a three-part structure of the associated coronal mass ejection that was observed to erupt on 2010 June 13. By applying successive geometrical fits to the cavity morphology, we find that the cavity exhibited non-self-similar expansion in the lower corona, below $2.2 \pm 0.2 R_S$, which points to the spatial scale for the radius of the source surface where the coronal magnetic field lines are believed to become radial. Furthermore, the kinematic study of the erupting cavity captures both the “impulsive” and “residual” phases of acceleration along with a strong deflection of the cavity at $1.3 R_S$. We also discuss the role of driving forces behind the dynamics of the morphological and kinematic evolution of the cavity.

Key words: Sun: corona – Sun: coronal mass ejections (CMEs) – Sun: evolution

1. Introduction

Coronal mass ejections (CMEs) are one of the most energetic phenomena that occur in the solar atmosphere, which in turn may have severe space-weather impacts on Earth (Gosling 1993; Siscoe 2000; Daglis et al. 2004). Therefore, understanding the physical processes behind the initiation and triggering mechanism of CMEs has become the top priority in space-science research.

Observing the development of coronal cavities in lower coronal regions can provide intriguing clues to the genesis of CMEs. Cavities are believed to be the density-depleted cross section of magnetic flux ropes, where the magnetic field strength has attained a much higher value compared to the background corona (Low & Hundhausen 1995; Rachmeler et al. 2013). They are usually observed as dark ellipses or partial ellipses at the limb in white-light (Waldmeier 1970), soft X-ray (Vaiana et al. 1973), and extreme ultraviolet (EUV; Schmahl 1979) observations.

These cavities may remain stable for days or even weeks (Gibson & Fan 2006), and they manifest as one of the three-part structure of CMEs if they erupt (Fisher & Poland 1981; Illing & Hundhausen 1985; Hundhausen 1999; Yurchyshyn 2002; Marićić et al. 2004; Sterling & Moore 2004; Vršnak et al. 2004; Gibson & Fan 2006; Vourlidas et al. 2013; Howard et al. 2017). Therefore, the morphological and magnetic properties of coronal cavities hold clues to the state of the pre-eruptive equilibria and the triggering mechanism behind the CME initiation.

Earlier studies indicate that the initiation and main acceleration phase of CMEs mostly occurs below 2–3 solar radii

(R_S ; MacQueen & Fisher 1983; Chen & Krall 2003; Joshi & Srivastava 2011). Therefore, by the time CMEs evolve into the field of view (FOV) of the Large Angle and Spectromeric Coronagraph Experiment (LASCO) C2, which observes from $2 R_S$, the initiation and impulsive acceleration phase of most of the CMEs can no longer be captured.

The *PROBA2* (Santandrea et al. 2013) “Sun Watcher using APS and Image Processing” (SWAP) EUV imager (Halain et al. 2013; Seaton et al. 2013) provides an extended (54 arcmin) FOV of the lower solar atmosphere, which gives the opportunity to capture the evolution of erupting cavities up to $1.7 R_S$ (up to $1.9 R_S$ along the diagonal direction of the images) around the 17.4 nm wavelength bandpass. Apart from that, using the off-pointing ability of *PROBA2*, the SWAP FOV can be shifted in any direction in order to track coronal features of interest, up to more than $2 R_S$. Therefore, it fills the observational gap between 1 and $2 R_S$. When combined with LASCO C2/C3 white-light observations (Brueckner et al. 1995), this enables us to study the complete evolution of erupting cavities. The large FOV of SWAP observations has been used in several studies of large coronal structures, such as capturing the different phases of prominence eruptions (e.g., Mierla et al. 2013) and the evolution of a large-scale coronal pseudo-streamer in association with a cavity system (Guennou et al. 2016). SWAP observations have also been used in conjunction with the ground-based Mauna Loa Solar Observatory Mark-IV K-coronameter (Mk4: Elmore et al. 2003) to study the initiation phase of a two-stage eruptive event (Byrne et al. 2014).

Statistical studies have been made in order to distinguish the morphological characteristics of eruptive and non-eruptive

cavities (Forland et al. 2013). Using AIA 193 Å passband observations, Forland et al. (2013) studied the morphological structure of 129 EUV cavities and found that cavities with a teardrop-shaped morphology are more likely to erupt. On the other hand, the partial or complete eruption of white-light cavities that formed CMEs has been studied using the combined observations of MK4 and LASCO coronagraphs (Gibson & Fan 2006; Liu et al. 2007). Comparing the MK4 observations of pre-eruptive white-light cavities with those observed a few days before the eruption, Gibson & Fan (2006) found that the cavities show an increase in height in the days leading up to an eruption. However, due to the absence of multiple line-of-sight observations, they concluded that it is hard to determine whether those changes in cavity height are due to the true evolution of a rising cavity or the appearance of a higher portion of the three-dimensional (3D) cavity along the line of sight. Gibson et al. (2010) proposed an observationally constrained 3D cavity model that reproduced the observed cavity morphology reasonably well, as seen from the different viewpoints of the two *STEREO* spacecraft. However, the temporal evolution of roughly the same portion of the 3D cavity morphology, starting from its long-lived quiescent phase to the eruptive phase associated with CMEs, has not been previously reported.

In this work, we present a comprehensive study of a coronal cavity that exhibited an almost two-week-long quiescent phase on the visible solar disk and finally erupted from the northwest solar limb on 2010 June 13. Using *SDO/AIA* observations, Régnier et al. (2011) studied the spatial relationship of this coronal cavity together with its associated prominence structure during the pre-eruptive phase. They reported the presence of magnetic curvature forces that balance the gravitational force in order to hold the cold and dense plasma of the prominence material underlying the cavity. However, using multiple vantage-point observations from *SDO/AIA*, *STEREO A/B*, and the *PROBA2/SWAP* EUV imager during the long-lived quiescent phase and combining the FOVs of SWAP and LASCO C2/C3 during the eruptive phase, we study the complete evolution of the cavity with an objective to address the following key questions regarding the genesis of CMEs:

- (i) Does the morphological evolution of the quiescent cavity hold clues to the underlying magnetostatic equilibria of the cavity system?
- (ii) What determines the initiation height of CMEs?
- (iii) What are the conditions that can lead to a cavity eruption?
- (iv) How do EUV cavities seen in the lower corona evolve into the white-light cavities seen during CME eruptions?
- (v) How do the magnetic forces drive the “impulsive” and “residual” acceleration phases of the CME?
- (vi) Do the CMEs undergo significant deflection in the lower corona?
- (vii) Do CMEs exhibit self-similar expansion in the lower corona? If not, then what is the critical height above which the nature of expansion is self-similar?

To answer these questions, we have organized this paper as follows. In Section 2, we present the observations of a quiescent cavity. We discuss the dynamics of that cavity during the eruptive phase in Section 3. In Section 4, we present the results based on our analysis. Finally, we summarize and discuss the implications of these results in Section 5.

2. Observations of the Coronal Cavity during the Quiescent Phase

The evolution of the coronal cavity in the lower corona during the different stages in its quiescent phase was captured well by the *SDO/AIA* (Lemen et al. 2012), *STEREO SECCHI/EUVI* (Wuelser et al. 2004, Howard et al. 2008), and *PROBA2/SWAP* EUV imagers. The cavity was first observed on the northeast solar limb on 2010 May 30 in association with a northern polar crown filament (Figure 1). Over the period from 2010 May 30 to June 13, the cavity rotated across the solar disk and remained in a quiescent phase before its eruption on 2010 June 13 at around 6:30 UT close to the northwest solar limb.

In order to increase the visibility of coronal structures in the EUV images, we have used the normalized radial graded filter (Morgan et al. 2006), which removes the radial gradient from coronal images. Furthermore, we have applied a high-pass filter to the EUV images using the standard `unsharp mask.pro` routine to enhance the cavity morphology. In order to investigate the spatial association between the prominence material and the dark cavity, we have superimposed the image of the prominence structure observed in the 304 Å channel on top of the dark cavity as observed in the 193 Å, 195 Å, and 174 Å channels of AIA, EUVI, and SWAP, respectively (see Figures 1, 3, and 4).

Figure 1 shows the appearance of the dark cavity over the east solar limb as seen in the AIA 193 Å channel on 2010 May 30 within the FOV between 1.0 and 1.3 R_s . The polar crown prominence structure associated with this cavity system can be seen in AIA 304 Å channel observations (see panel (b) in Figure 1). In order to distinguish the true cavity from the outside region of dipped field lines which carry the prominence material, we have marked the cavity morphology, as observed in the AIA 193 Å image, with the green dotted boundary drawn on the superimposed co-temporal images taken in the AIA 193 and 304 Å channels (see panel (c) in Figure 1). Here we refer to the “true” cavity as the central nondipped part of the magnetic flux rope following the classification described in Gibson (2015). The combined images of the prominence structure and the cavity morphology, seen in Figure 1, indicate that the cavity is located exactly on the top of the prominence boundary. The yellow dotted elliptical boundary outside the dark cavity approximately encloses the outer boundary of the flux rope. Outside the yellow dotted boundary, the bright arch-like structures resemble the overlying magnetic field lines.

During its passage across the solar disk, the polar crown filament was well observed from multiple viewpoints of *SDO*, *PROBA2*, and the twin spacecraft *STEREO A* and *B*. As it passed close to the central meridian, as seen from the perspective of Earth, the associated cavity morphology became visible in the plane-of-sky (POS) EUVI observations from the *STEREO* satellites. At that time, *STEREO A* and *B* were positioned approximately 70° from the Sun–Earth line (see Figure 2). On 2010 June 4, the cavity appeared in the POS from the perspective of *STEREO A* (Figure 3), which was approximately 18° east of the Sun–Earth line (see Figure 2). Between 2010 June 4 and 7, the cavity crossed the solar disk center as viewed from Earth and rotated about 20° farther from the Sun–Earth line toward the west. At around 14:00 UT on 2010 June 7, it became visible in POS EUVI observations from *STEREO B*. Figure 3 shows the appearance of the dark cavity and the associated prominence structure as observed from the

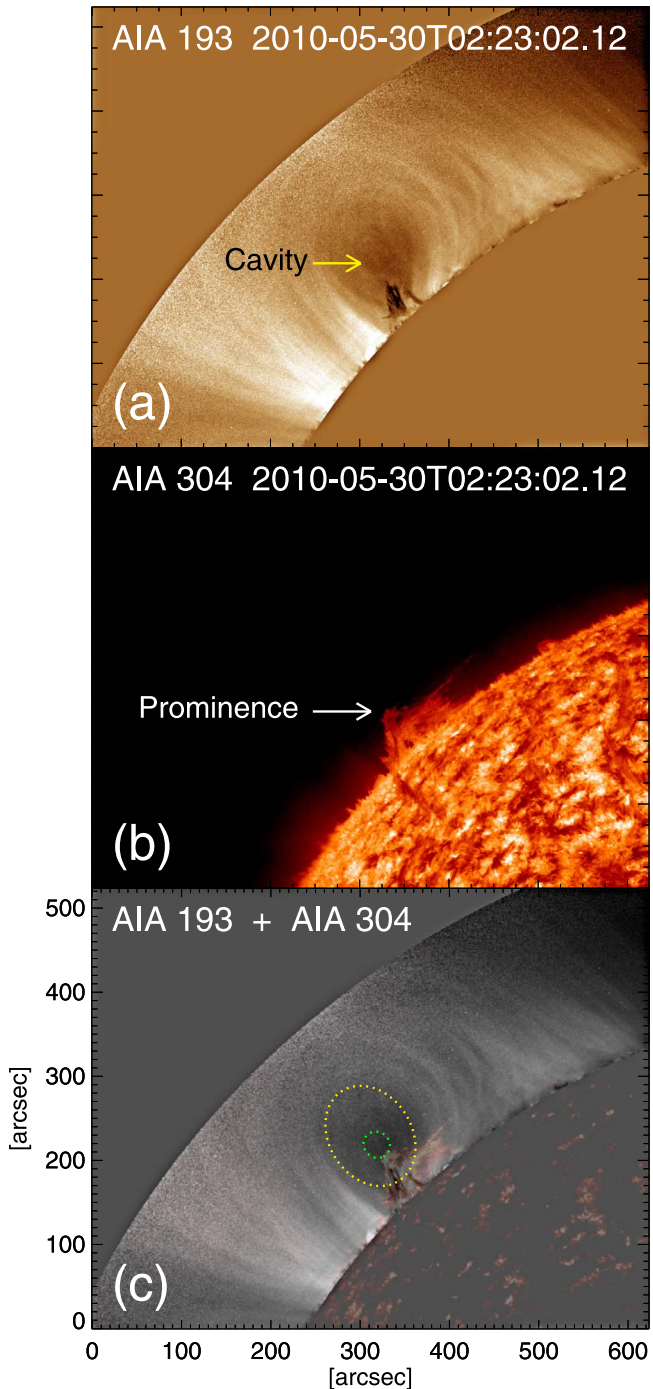


Figure 1. Observation of the coronal cavity in the AIA 193 Å channel (a). The associated prominence structure as seen in the AIA 304 Å channel (b). The superimposed images of panels (a) and (b) are shown in panel (c). The green dotted line denotes the outer boundary of the true cavity. The yellow dotted line depicts the approximate outer boundary of the flux rope.

two perspectives of *STEREO A* and *B* in the 195 Å (top panels) and 304 Å (middle panels) bandpasses, respectively. The green and yellow dotted boundaries, highlighting the true cavity and flux rope outer boundaries, respectively, drawn on the superimposed images (bottom panels of Figure 3) are the same as those described for Figure 1.

As the filament rotated toward the west solar limb, the associated cavity started to appear on the northwest solar limb

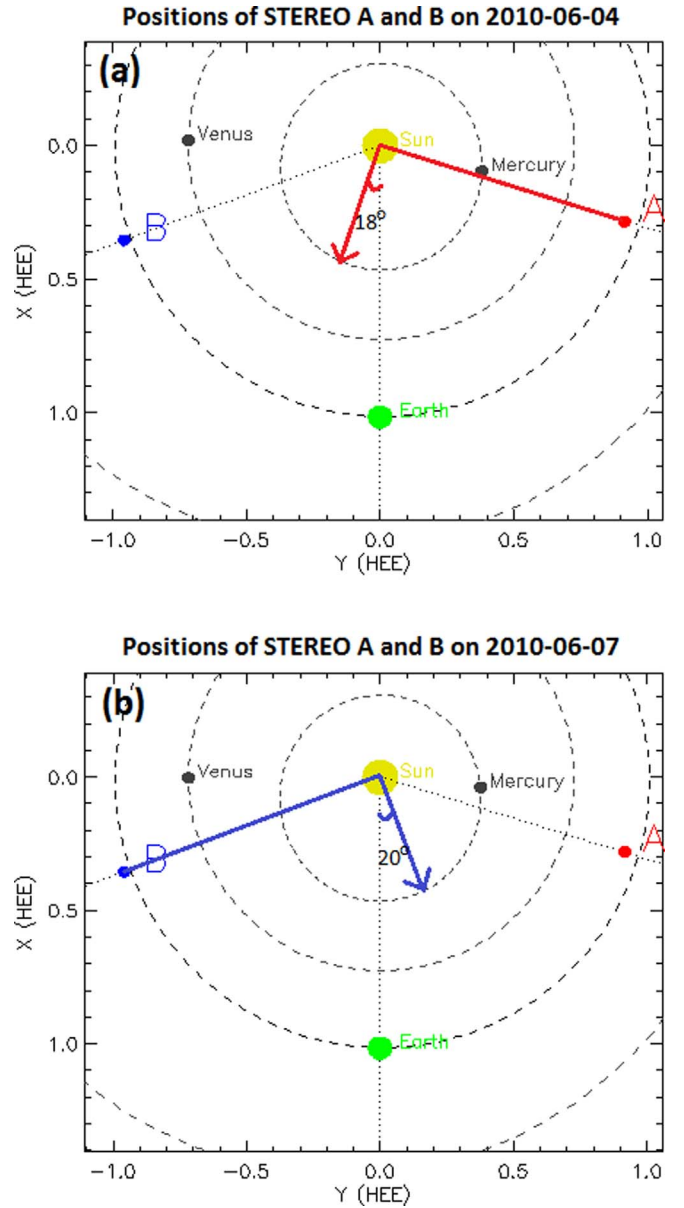


Figure 2. Positions of *STEREO A* and *B*. The red and blue arrows drawn in panels (a) and (b) denote the direction of the plane of sky as viewed by EUVI on 2010 June 4 by *STEREO A* and on 2010 June 7 by *STEREO B*.

as viewed from the perspective of Earth. The cavity can be observed from 2010 June 11 and is clearest at the end of 2010 June 12. Figure 4 shows the cavity morphology as observed in SWAP 174 Å (left panel), the associated prominence structure in AIA 304 Å (middle panel), and a combination of both bandpasses (right panel). As one of the major goals of this paper is to track the complete evolution of the eruptive cavity, we take advantage of SWAP's large FOV and ability to track the cavity out to $\approx 1.7 R_S$ (compared to the AIA FOV which is limited to $1.3 R_S$), and focus on SWAP observations throughout the cavity evolution from the quiescent to eruptive phase on the northwest solar limb. In order to increase the signal-to-noise in the far field of the SWAP images, the 1.6 minute cadence images between 00:00 UT and 01:35 UT on 2010 June 13 have been processed using a median stacking technique to capture the cavity morphology before eruption. Finally, the

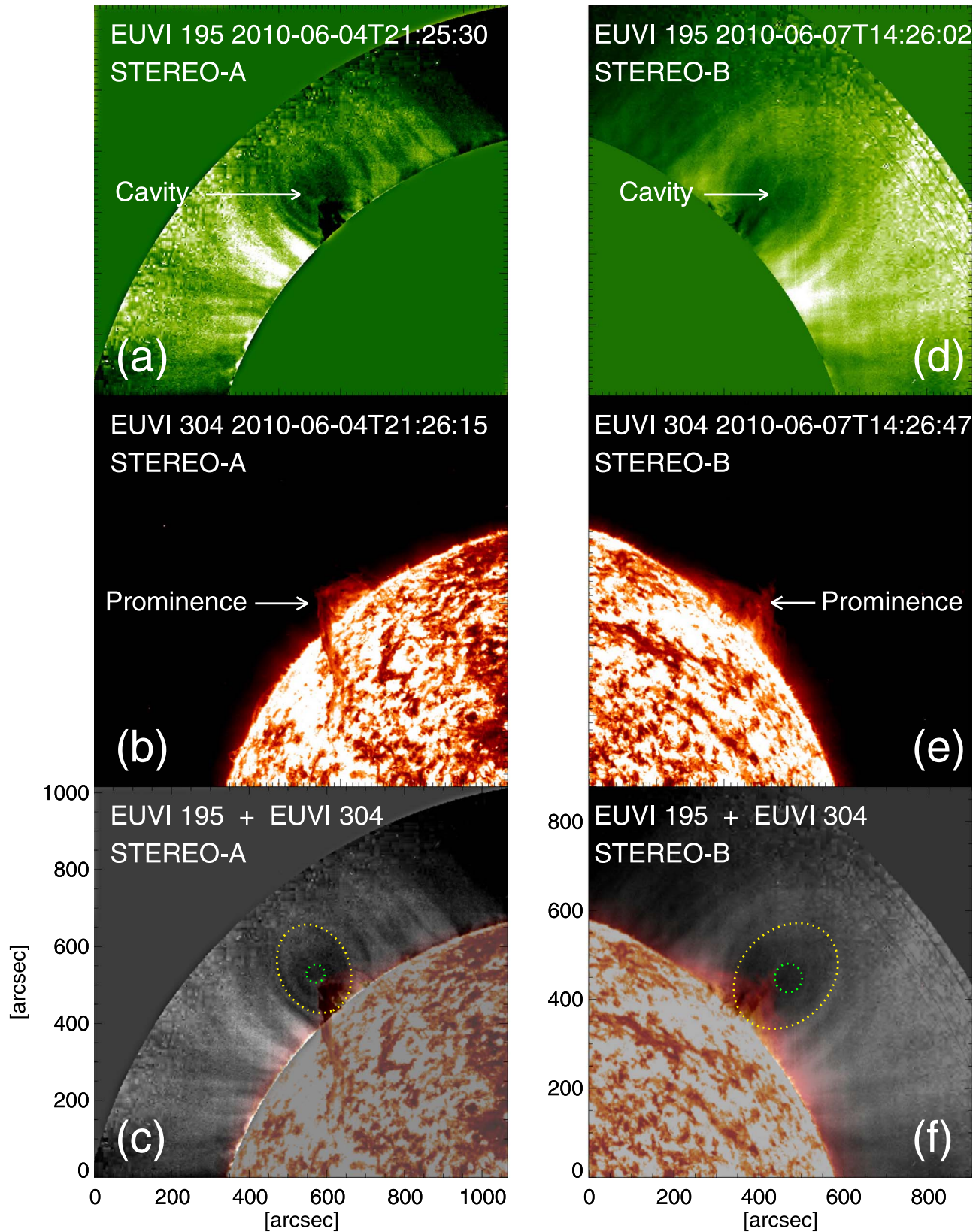


Figure 3. Observations of the coronal cavity as seen in the 195 \AA bandpass of EUVI on STEREO A and B (panels (a) and (d), respectively), the associated prominence structure in the 304 \AA bandpass (panels (b) and (e)), and a superposition of the 195 \AA and 304 \AA bandpasses (panels (c) and (f)). The green and yellow dotted lines are the same as those described for Figure 1.

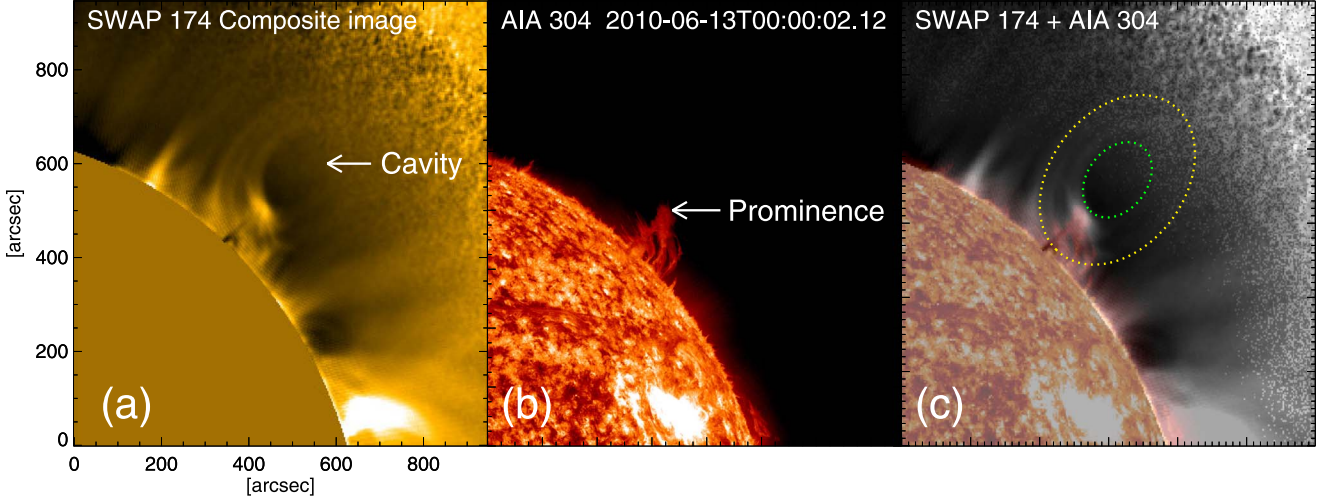


Figure 4. Observations of the coronal cavity as viewed in SWAP composite images (a) and the associated prominence structure as seen in the AIA 304 Å channel (b). The superimposed images of the cavity morphology and the prominence structure as depicted in panels (a) and (b) are shown (c). In panel (c), the background image in grayscale represents the cavity morphology as depicted in panel (a), and the foreground image in AIA 304 Å color scale represents the prominence structure as shown in panel (b). The green and yellow dotted lines are the same as those described for Figure 1.

cavity erupted at around 06:30 UT from the northwest solar limb as viewed by Earth and evolved into a CME as observed in LASCO C2/C3 images.

In order to associate the morphological evolution of the EUV cavity with that of the three-part structure of the associated CME seen in white-light observations, it is important to understand whether or not the cross-sectional profiles of the cavity, as observed in EUV and white-light images, resemble the same morphological structure. Comparing the EUV and white-light observations of an erupting loop system that formed a CME, Byrne et al. (2014) found an inconsistency between the evolutionary profiles of the erupting structure as seen in EUV and white-light images. It is important to note that the white-light observations, which capture the Thomson-scattered light from the free electrons of the solar corona, are dependent on the electron density and are more sensitive to features near the POS (Vourlidas & Howard 2006; Howard & DeForest 2012; Inhester 2015), whereas the EUV observations are primarily sensitive to both the temperature and density of the plasma (Martínez-Sykora et al. 2011; Del Zanna & Mason 2018), and are less preferentially sensitive to features based on their location with respect to the POS, as is the case for white-light coronagraph images. Therefore, any coronal feature, such as the erupting loop system studied in Byrne et al. (2014), that lies away from the POS will appear as different morphological structures in EUV and white-light observations.

Coronal cavities are extended tunnel-like structures that are mostly associated with the polar crown filaments (Gibson 2015). When these large structures line up along the line of sight, they appear like a dark croissant-like feature in the POS observations due to the density depletion in comparison to the surrounding corona. In particular, any portion of the cavity is best seen when it lies on the POS (Gibson et al. 2010). Therefore, the line-of-sight integrated Thomson-scattered brightness, as obtained by the white-light coronagraphs, and the line-of-sight integrated EUV emission as obtained by SWAP or AIA in the 174 Å and 193 Å passbands, which are also sensitive to the electron density, due to the presence of Fe IX and Fe XII emission lines (Martínez-Sykora et al. 2011), should have identical morphologies for any observed coronal

cavity. In order to validate this, we have compared the SWAP EUV observations of the cavity morphology with the white-light observations as obtained from the Mk4 coronagraph, which observes between 1.1 and 2.8 R_S .

Panel (b) in Figure 5 shows the cavity morphology as seen in the daily averaged polarized brightness observations obtained from the ground-based Mk4 coronagraph on 2010 June 13. The green crosses in panel (b) approximately indicate the outer boundary of the white-light cavity embedded in a coronal streamer. The same green crosses have been overplotted on the SWAP EUV image in panel (a), which clearly shows that the EUV and white-light cavity morphologies are the same. Furthermore, using an observationally constrained 3D cavity model (Gibson et al. 2010), we have FORWARD-modeled (Gibson et al. 2016) the cavity morphology in both the EUV emission lines and the Thomson-scattered polarized brightness. The line-of-sight integrated EUV emission in the 174 Å passband (panel (c)) and the Thomson-scattered polarized brightness (panel (d)) has been obtained using the model density and temperature of the coronal cavity, embedded in a coronal streamer (Gibson et al. 1999). The similarity between the cavity morphologies seen in the synthesized EUV and white-light images reveals that both the EUV and white-light cavities possess a fundamentally identical morphology, co-located in a large 3D structure.

3. Evolution of the Coronal Cavity during the Eruptive Phase

3.1. Morphological Evolution of the Cavity

The cavity morphology as observed in the SWAP EUV image is best fitted with the elliptical boundary where the cavity centroid reached a height of $\approx 0.23 R_S$ above the solar surface at approximately 00:00 UT on 2010 June 13, prior to the eruption (see Figure 6).

Although the cavity boundary is clearly detectable in the SWAP composite images, it is difficult to detect the full outer boundary of the cavity in each individual SWAP image. Only the lower boundary of the cavity can be identified, due to the emission from the lower lying prominence material which acts

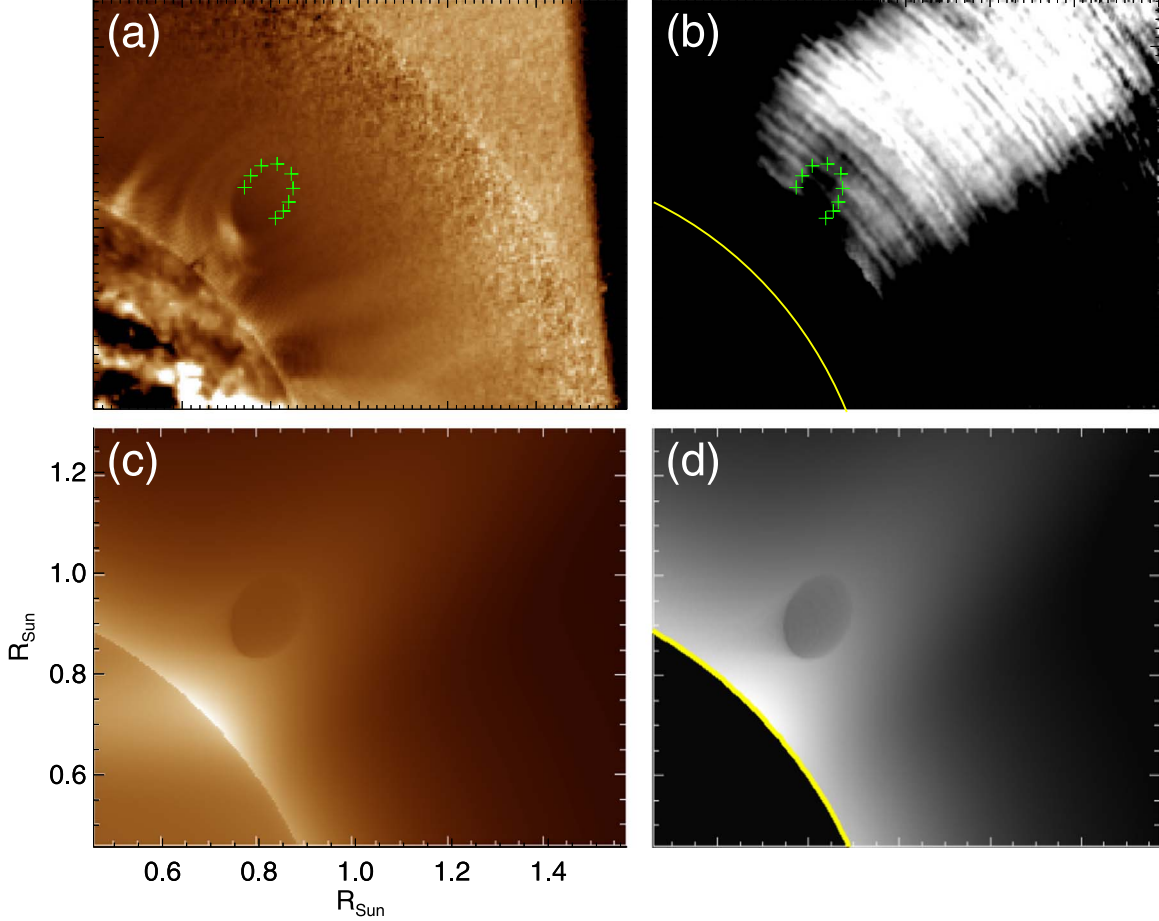


Figure 5. Cavity morphology as seen in SWAP composite images stacked over the period between 00:00 UT and 01:35 UT on 2010 June 13 (a). The daily averaged polarized brightness as imaged by the ground-based coronagraph MK4 on 2010 June 13 (b). The green crosses in panel (b) approximately indicate the outer boundary of the white-light cavity embedded in a coronal streamer. The same green crosses shown in panel (b) have been drawn on panel (a). FORWARD-modeled (line-of-sight integrated) EUV emission in the 174 Å passband (c) and the white-light polarized brightness (d) using the model density and temperature of the cavity embedded in a coronal streamer.

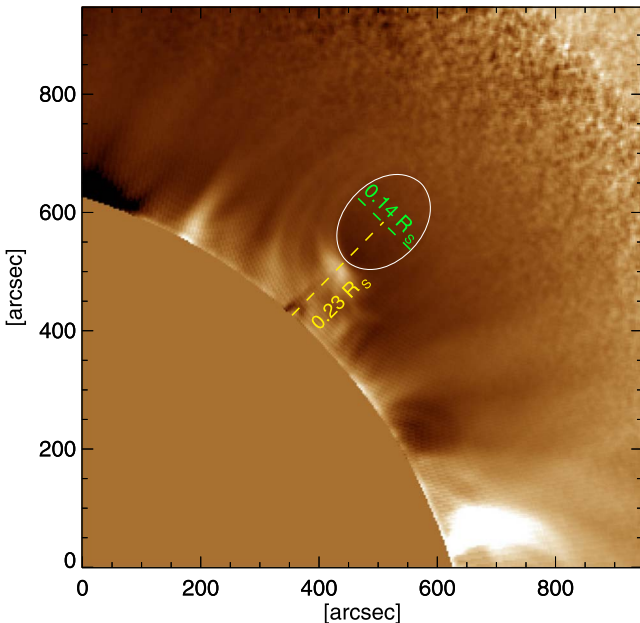


Figure 6. Cavity morphology as seen in SWAP composite images stacked over the period between 00:00 UT and 01:35 UT on 2010 June 13. The cross-sectional dimension of the cavity and the distance to the cavity centroid from the solar surface are indicated.

as the outer boundary of the cavity. Therefore, we have traced the coordinates along the lower half boundary of the cavity structure at different times throughout its eruption. These traced coordinates are then fitted with an elliptical geometry, assuming that the upper part of the cavity morphology is symmetrical like the lower half (see Figure 7). Figure 8 depicts the morphological evolution of the cavity within SWAP FOV where each of the ellipses represents the geometrically fitted structure of the cavity morphology at different time steps during its eruptive phase as shown in Figure 7.

In order to understand how the EUV cavity at the lower corona evolved into the white-light cavity associated with the CME, we have combined the SWAP observations with the white-light coronagraphic images as captured by LASCO C2/C3. Figure 9 depicts the transformation of the cavity from the EUV to white-light observations, and its evolution as a three-part structure of the associated CME. In order to capture the complete evolution of the cavity, we also apply the geometrical fitting to the white-light cavity morphology. The outer boundary of the dark cavity on the top of the bright filament as observed in LASCO C2/C3 has been fitted up to a height of $8 R_S$. Beyond $8 R_S$, the cavity morphology became too diffused to be fitted with certainty. It was possible to track the centroid of the EUV cavity out to $1.8 R_S$ using the morphological fit to its lower boundary, even when the cavity centroid height

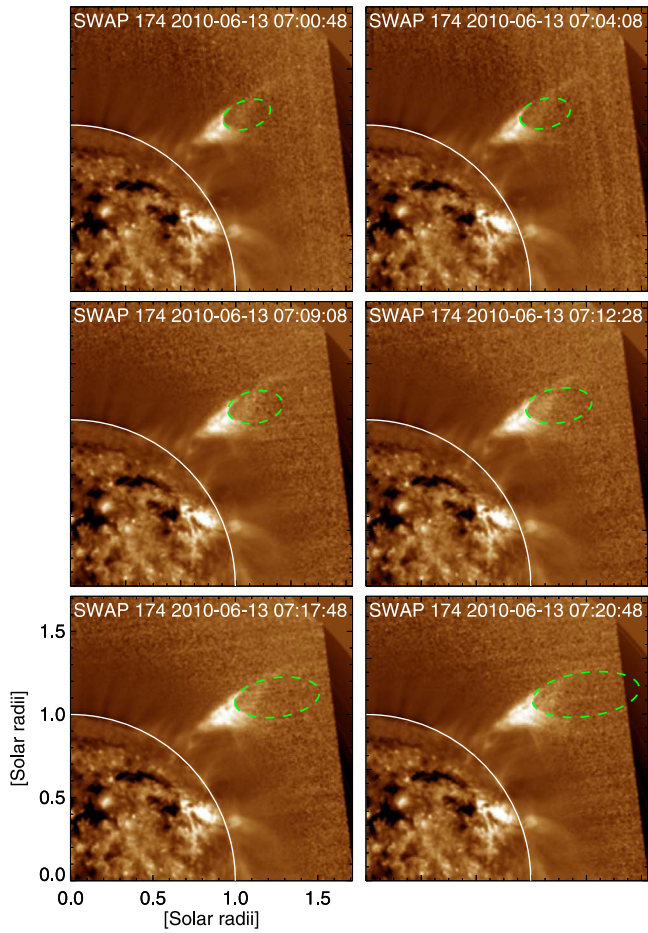


Figure 7. Cavity morphology as observed in the SWAP EUV images during the eruptive phase. The solid white line in each panel highlights the position of the solar limb. The green dashed ellipses depict the geometrical fit to the cavity morphology.

exceeded the outer extent of the SWAP FOV. Similarly, we have fitted the upper half of the white-light cavity in the LASCO FOV for several frames where the lower part of the cavity was obscured by the occulter and the cavity centroid height resided below $2 R_S$. Therefore, the small observational gap (1.8 to $2 R_S$) between the SWAP and LASCO FOV did not affect the continuous tracking of the erupting cavity. The morphological evolution of the coronal cavity starting from its initial centroid height at $1.23 R_S$ up to $8 R_S$ can be seen in Figure 10.

3.2. Kinematic Evolution of the Cavity–Prominence System

As discussed in Section 2, during the quiescent phase, the spatial association between the prominence structure and the cavity morphology shows that the prominence material lies exactly at the bottom of the cavity (see Figures 1, 3, and 4). In order to investigate whether this spatial relationship is also maintained during the eruptive phase, we have separately tracked the top boundary of the prominence material as observed in the AIA 304 Å channel and the bottom boundary of the coronal cavity as observed in SWAP EUV images. This was done by placing a slit at a position angle of 317° on both the SWAP and AIA images, and stacking the evolution of the cavity and filament boundary with time within the respective

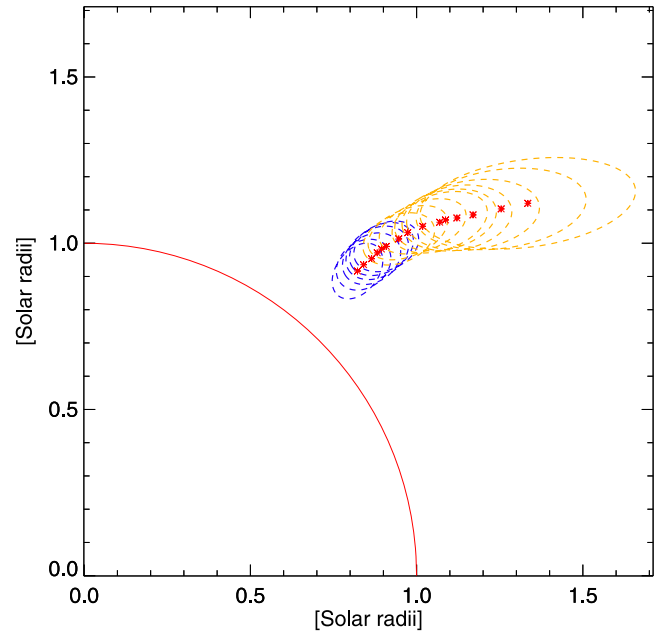


Figure 8. Morphological evolution of the cavity system within the SWAP FOV during the eruptive phase. The red boundary highlights the solar limb. The blue dotted ellipses denote the geometrical fit to the cavity morphology during the radial motion within $1.3 R_S$, whereas the yellow dotted ellipses denote the same during the nonradial motion after the deflection at $\approx 1.3 R_S$. The red asterisks depict the trajectory of the cavity centroid.

slits. Figure 11 shows the position of the slits (top panels) in the SWAP EUV and AIA 304 Å images. The bottom panels of Figure 11 illustrate the evolution of the bottom boundary of the cavity (panel (c)) and the top boundary of the filament (panel (d)). In order to compare these two height–time profiles, we have selected the points with proper coordinate information along the two height–time curves as marked by the square diamond shaped symbols drawn on the two time-slice diagrams (Figure 11). These selected points along the two height–time curves are then overplotted in Figure 12. The error bars ($\pm 0.006 R_S$) are a measure of the uncertainty in selecting the points along the curve boundary.

4. Results

4.1. Spatial Relation between the EUV Cavity and the Associated Prominence

Combining the observations of the erupting cavity and the associated prominence structure, we have studied the spatial relationship between them in lower corona during both the quiescent and eruptive phases. Figure 12 clearly shows that the height–time profiles of the filament top and the cavity bottom boundary coincide with each other. This indicates that throughout the eruptive phase, the cavity is located exactly on top of the prominence, which is in agreement with the understanding of the classical three-part structure of CMEs.

4.2. Cavity Morphology during the Quiescent Phase

By using multispacecraft observations from *SDO*, *STEREO*, and *PROBA2*, we have tracked the gradual evolution of the stable EUV cavity at different times during its passage across the solar disk.

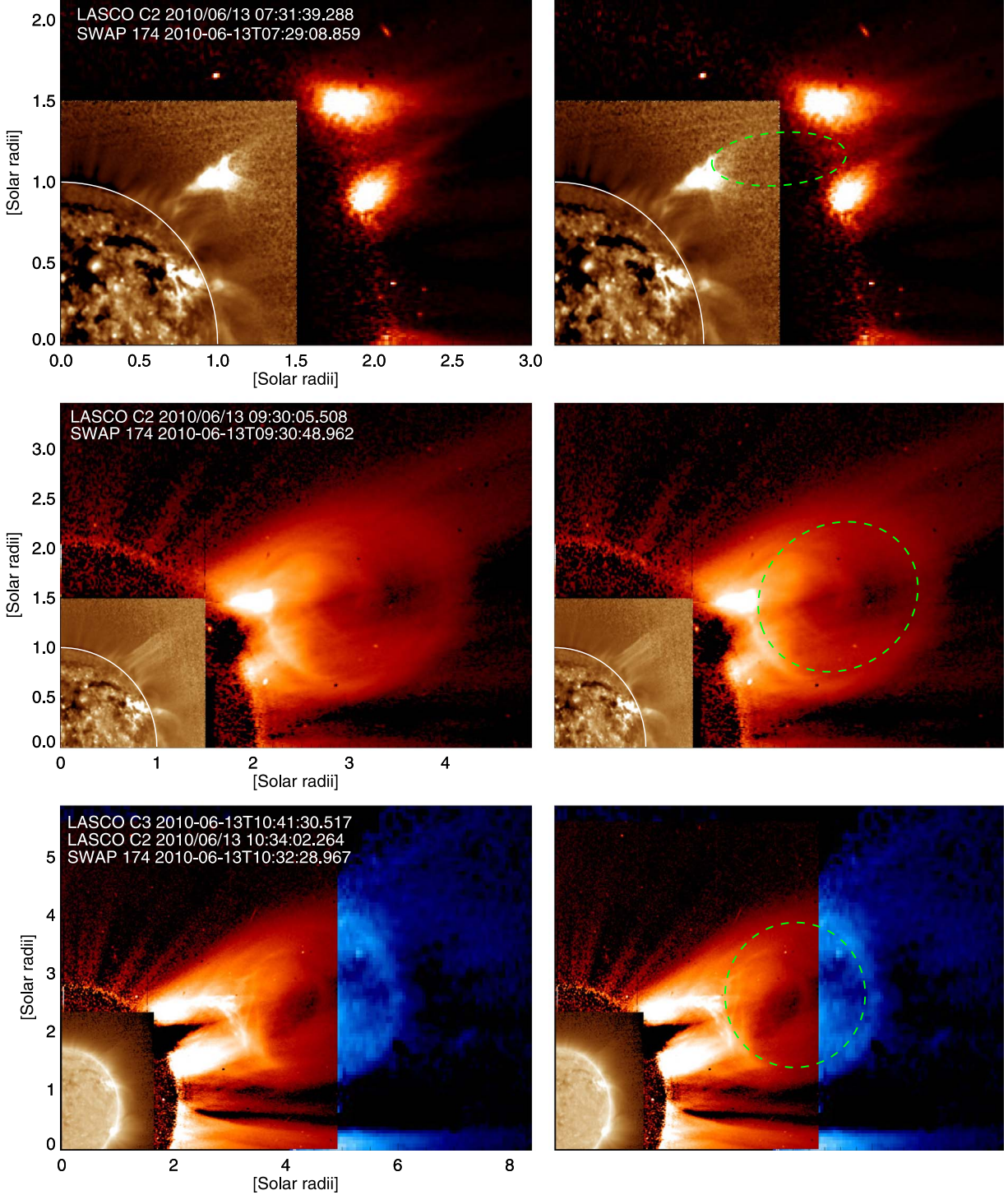


Figure 9. Cavity morphology as observed in white-light coronagraphic images of LASCO C2 and C3 observations (red and blue, respectively), with SWAP observations superimposed in the center. The white solid lines highlight the solar limb. The green dashed lines show the geometrical fit to the cavity morphology.

However, in order to relate the different evolutionary phases of the quiescent cavity, it is important to track the same portion of the large 3D structure associated with it. Figure 13 shows the location of the associated H α filament channel on 2010 June 6, when it was close to the solar disk center. The longitudinal extent of the filament channel was approximately 60°, and the Carrington heliographic longitude of the central part (indicated by the yellow star in panel (a) of Figure 13) of this long filament channel was 132° ± 4°. Noticeably, the Carrington

longitude of the quiescent cavity system on 2010 May 30 and June 4, 7, and 13 as observed sequentially by the *SDO*, *STEREO A*, *STEREO B*, and *PROBA2* was 136°, 132°, 134° and 132°, respectively (see Table 1), which was nearly the same as the Carrington longitude of the central part of the filament channel. Moreover, as the orientation of the filament channel was nearly horizontal with respect to the solar equator, the associated flux rope possessed a close to azimuthally symmetric structure with respect to the solar rotational axis.

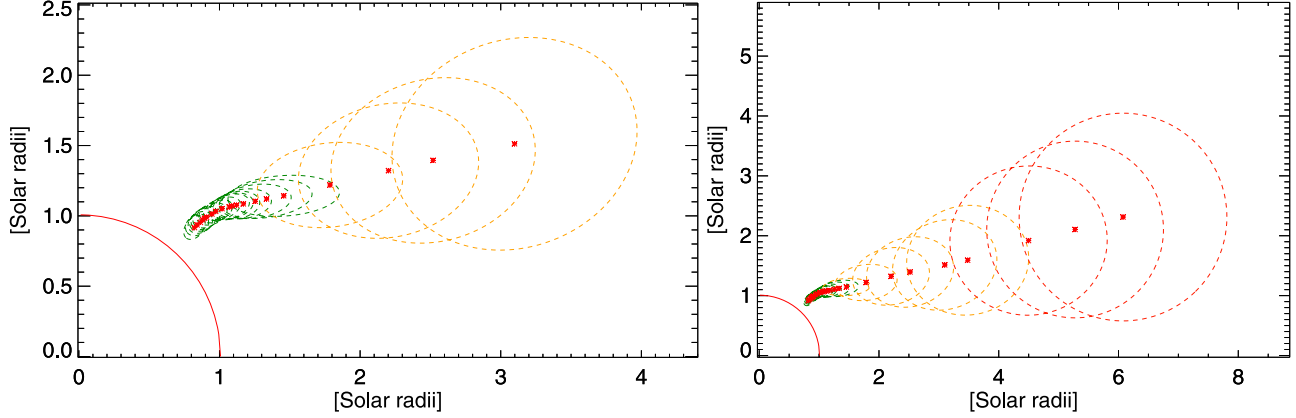


Figure 10. The left panel shows the geometrical fit to the cavity morphology observed in the combined FOV of SWAP (green ellipses) and LASCO C2 (yellow ellipses). The right panel shows the geometrical fit to the cavity morphology observed in the combined FOV of SWAP (green dotted ellipses), LASCO C2 (yellow dotted ellipses), and LASCO C3 (red dotted ellipses). The red solid boundary highlights the solar limb. The red asterisks depict the trajectory of the cavity centroid.

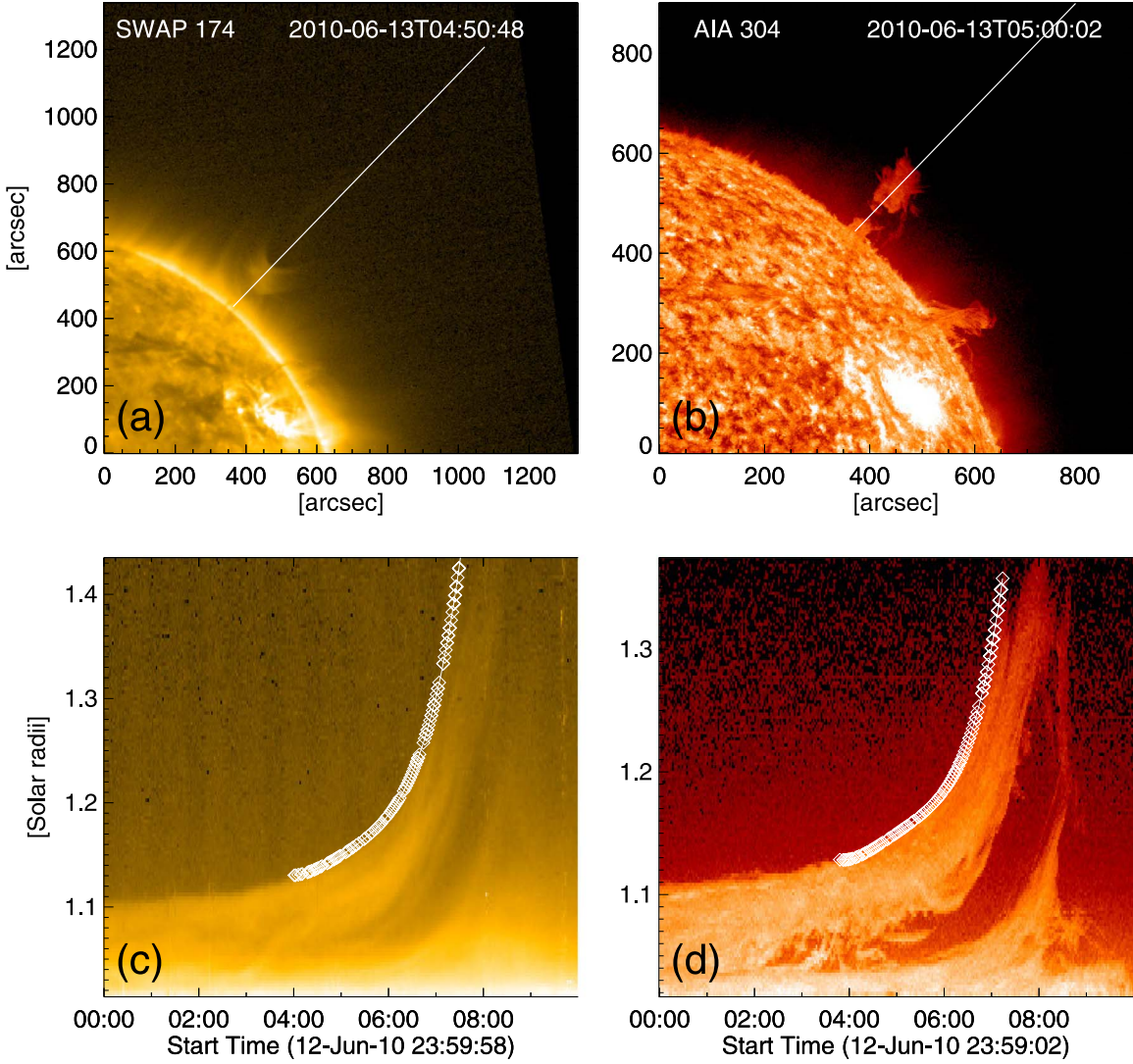


Figure 11. The position of the slits superimposed on the SWAP and AIA images (panels (a) and (b), respectively) along with the height–time profiles for the lowest boundary of the cavity (c) and the topmost part of the prominence (d).

Therefore, all of the observations depicting the different phases of the quiescent cavity capture the same part of the large 3D structure and hence reveal the true evolution of the cavity during its long-lived quiescent phase.

The geometrical fit to the cavity structure reveals that the cavity boundary had a nearly circular morphology when it appeared on the east solar limb, and it still had this shape when it was positioned near disk center, as seen from the POS EUVI

Table 1
Cavity Morphology throughout the Quiescent Phase

Observation Time yyyy/mm/dd hh:mm:ss	Observing Instrument	Longitude of the Cavity in Stonyhurst/Carrington Heliographic Coordinates	Cavity Centroid Height (R_S)	Cavity Morphology	Cavity Diameter (R_S)
2010 May 30 02:32:02	<i>SDO/AIA</i>	90° E/136°	1.10	≈Circular	0.016 ± 0.002
2010 Jun 4 21:25:30	<i>STEREO A/SECCHI EUVI</i>	18° E/132°	1.13	≈Circular	0.039 ± 0.008
2010 Jun 7 14:26:02	<i>STEREO B/SECCHI EUVI</i>	20° W/134°	1.17	≈Circular	0.054 ± 0.008
2010 Jun 13 04:00:00	<i>PROBA2/SWAP</i>	90° W/132°	1.23 ± 0.02	Elliptical	0.09 ± 0.02

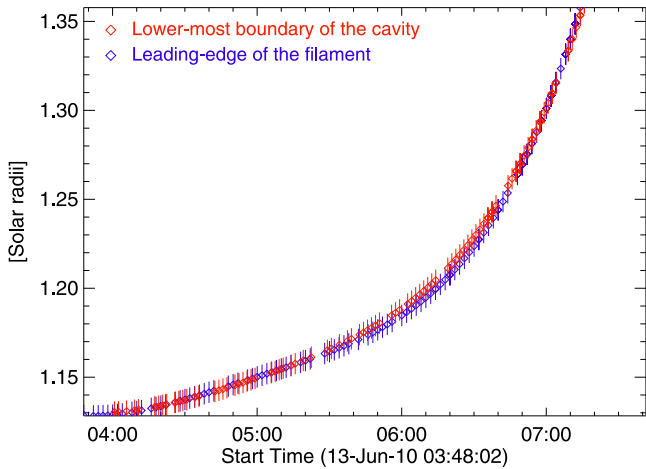


Figure 12. The height–time profiles of the lowest boundary of the cavity (red) and the leading edge of the filament (blue), as recorded in Figure 11.

observations of *STEREO A* and *B* (see Figures 1 and 3). However, the cavity morphology evolved into a more elliptical shape as it approached the west solar limb, prior to eruption (see Figure 4). Apart from the morphological change, the quiescent cavity also undergoes a slow rise and expansion phase. As the cavity rotated across the solar disk from the east to west solar limb, its diameter increased from 0.016 ± 0.002 to $0.09 \pm 0.02 R_S$ and the cavity centroid height rose from 1.10 to $1.23 \pm 0.002 R_S$ (see Table 1) before it finally erupted from the west solar limb.

4.3. Cavity Dynamics during the Eruptive Phase

Using the large FOV of SWAP, we have sequentially captured the evolution of the erupting cavity morphology in the lower corona up to $1.7 R_S$. Figure 8 presents a clear depiction of a significant nonradial motion exhibited by the cavity at about $1.3 R_S$, where its position angle changed from approximately 310° to 270° . In general, the equatorward deflection of CMEs is believed to be due to the influence of polar coronal holes (Cremades et al. 2006; Panasenco et al. 2011). However, the EUV images obtained from the AIA and SWAP on 2010 June 13 do not show any signature of a polar coronal hole in the northern hemisphere, which may be due to the line-of-sight tilt of the solar magnetic axis. Therefore, in order to identify the presence of a polar coronal hole, we have used EUV observations of the Sun on the same day from the perspective of *STEREO A* (see the position of *STEREO A* in Figure 2).

Panel (b) in Figure 13 clearly shows the presence of a northern polar coronal hole on 2010 June 13 as observed by

STEREO A EUVI in the 195 \AA passband. In order to identify the location of the filament channel on the EUVI 195 \AA image, we first computed the Carrington longitude and latitude of the points along the $\text{H}\alpha$ filament channel (indicated by the red solid line in panel (a) of Figure 13) as observed on 2010 June 6. Using the information on the Carrington heliographic coordinates of these points, the same filament channel has been overlaid on the *STEREO A EUVI* 195 \AA image. The location of the filament channel in the vicinity of the northern polar coronal hole reveals that the open magnetic field lines originating from the polar coronal hole might have channeled the trajectory of the erupting cavity toward the heliospheric current sheet. Therefore, the cavity deflected from a higher latitude to a lower one.

By combining the observations from SWAP and LASCO C2/C3, we have studied the association between the EUV and white-light observations of the cavity. Figure 10 shows that during the eruptive phase, the cavity morphology gradually evolved from an initial elliptical shape to a semi-circular one (see the left panel of Figure 10) within the FOV of LASCO C2. As the cavity evolved further, it became almost circular after about $4 R_S$. Noticeably, after the initial deflection at about $1.3 R_S$, the cavity maintained the same position angle (270°) throughout the rest of its propagation trajectory.

4.4. Nature of Expansion of the Erupting Cavity

In order to investigate whether or not the cavity evolution was self-similar, we have plotted the evolution of the cavity aspect ratio with respect to the cavity centroid height. The numerator of the aspect ratio is the length of the semimajor axis of the cavity ellipse and the denominator is the distance from Sun center to the cavity centroid along the nonradial trajectory of the cavity propagation.

The upper panel of Figure 14 shows the evolution of the cavity width to the centroid height aspect ratio, which can be seen to gradually increase to 0.25 ± 0.03 at $2.2 \pm 0.2 R_S$, after which it became approximately constant for the remainder of its propagation. This clearly shows that within $2.2 \pm 0.2 R_S$, the cavity exhibited non-self-similar expansion whereas beyond $2.2 \pm 0.2 R_S$, it enters into a regime of self-similar expansion. The non-self-similarity in the cavity evolution is also reflected in its expansion profile in the lower corona. The bottom panel of Figure 14 shows that the cavity diameter (length along the major axis of the ellipses fitted to the cavity morphology) expands linearly after $2.2 \pm 0.2 R_S$, whereas it evolves in a different fashion within the non-self-similar regime in lower corona. Noticeably, this critical height ($2.2 \pm 0.2 R_S$) resembles the radius of the source surface (2.5 ± 0.25) where the coronal magnetic field lines are believed to become radial (Hoeksema 1984).

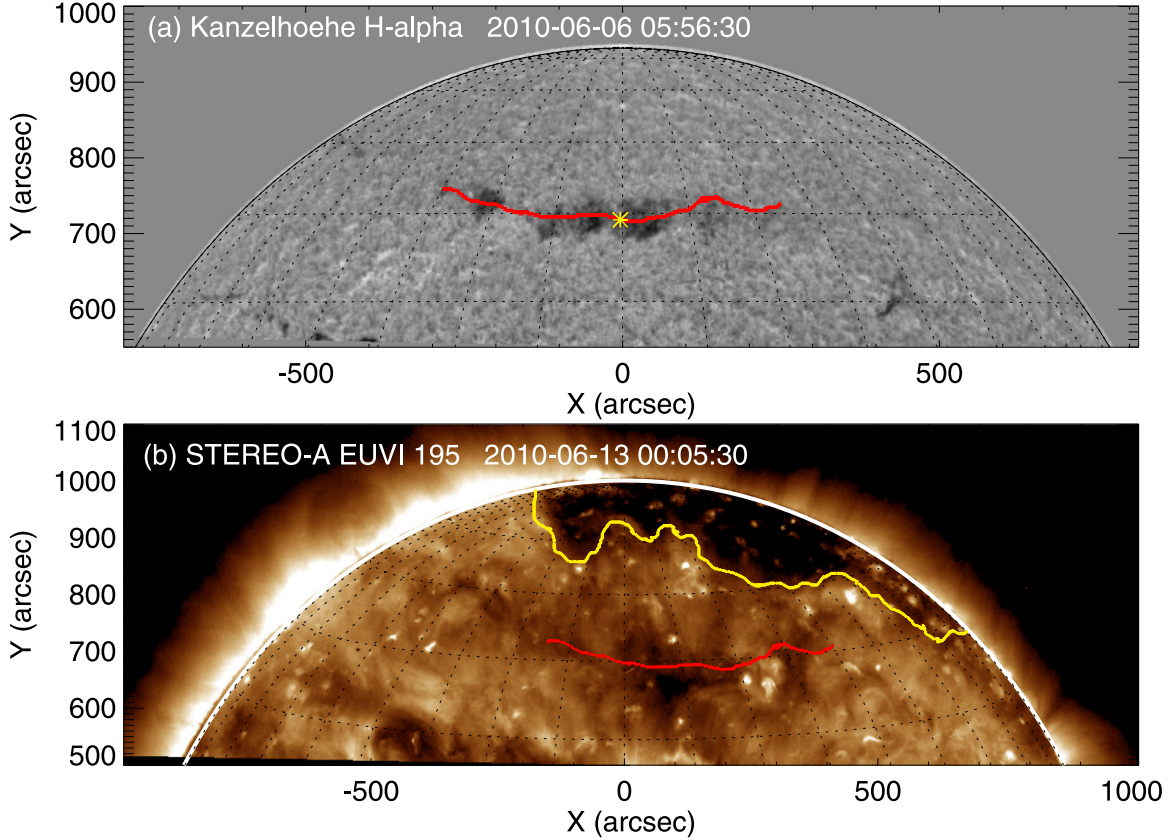


Figure 13. H α image of the polar crown filament on 2010 June 6 (a). The red solid line, drawn over the image, depicts the approximate position of the filament channel on the solar disk. The yellow star approximately locates the central part of the long filament channel. STEREO A EUVI 195 \AA image on 2010 June 13 (b). The yellow solid line denotes the boundary of the northern polar coronal hole. The red solid line in panel (b) indicates the location of the same filament channel as shown in panel (a).

4.5. Kinematic Evolution of the Cavity

Investigating the kinematics of the erupting cavity, we find that the individual height-time profiles of the cavity top, centroid, and bottom evolve in a different manner, due to the internal expansion of the cavity structure (panel (a) of Figure 15). Interestingly, the velocity profiles shown in Figure 15 depict that the erupting cavity undergoes two distinct phases of kinematic evolution.

During the first phase, the speed of the top, centroid, and bottom of the cavity quickly reached approximately 350, 250, and 150 km s^{-1} , respectively, within $\approx 1.8 R_{\odot}$. However, the second phase of the kinematic evolution starts after $2 R_{\odot}$ where the speed of the three different parts of the cavity increases more gradually in comparison to the first kinematic phase. Noticeably, the cavity centroid exhibited peak acceleration at $1.67 \pm .08 R_{\odot}$, where the top, center, and bottom parts of the cavity attained the accelerations of 345 ± 15 , 234 ± 11 , and $124 \pm 6 \text{ m s}^{-2}$, respectively. This impulsive phase of acceleration is believed to be governed by the Lorentz self-force where the outward magnetic pressure dominates over the external and/or internal magnetic tension force (Byrne et al. 2010). Importantly, the peak acceleration height ($1.67 \pm 0.08 R_{\odot}$) of the cavity obtained in this study is in agreement with the mean value ($1.72 R_{\odot}$) of that found for the filament-associated CMEs studied by Bein et al. (2012). However, after $2 R_{\odot}$, the average acceleration reduces to below 50 m s^{-2} , which is believed to be the “residual acceleration phase” of the CME where the Lorentz

self-force undergoes the declining phase and the flux rope dynamics become strongly dependent on the drag force (Chen & Krall 2003).

In order to initiate the first phase of the kinematic evolution, several triggering mechanisms have been proposed (see the review by Chen 2011). Catastrophic loss of equilibrium, ideal MHD instabilities, tether cutting, magnetic breakout, triggering by flux emergence or cancellation, and mass drainage are believed to be one of the possible driving mechanisms for triggering the initial acceleration phase. Interestingly, by fitting the height-time profiles of the kinematic evolution with a power-law polynomial and by comparing it with the results obtained from different numerical simulations, one may get clues to the underlying eruption mechanism (Török & Kliem 2005; Williams et al. 2005; Mierla et al. 2013).

Schrijver et al. (2008) have shown that the rapid acceleration phases of erupting prominences are best characterized by a height-dependent function, $h(t) \propto t^m$, where $h(t)$ is the instantaneous height at any time t and m is the power-law exponent. Using this power-law function, we have fitted the height-time profile of the cavity centroid during its impulsive acceleration phase in between 06:40 to 07:30 UT on 2010 June 13. The red dashed line in panel (c) of Figure 15 shows the curve of best fit obtained by using $m = 3.6$. Noticeably, an exponent value (m) close to 3 corresponds to the torus instability scenario (Schrijver et al. 2008). Therefore, our results suggest that the impulsive acceleration phase was most likely driven by the torus instability.

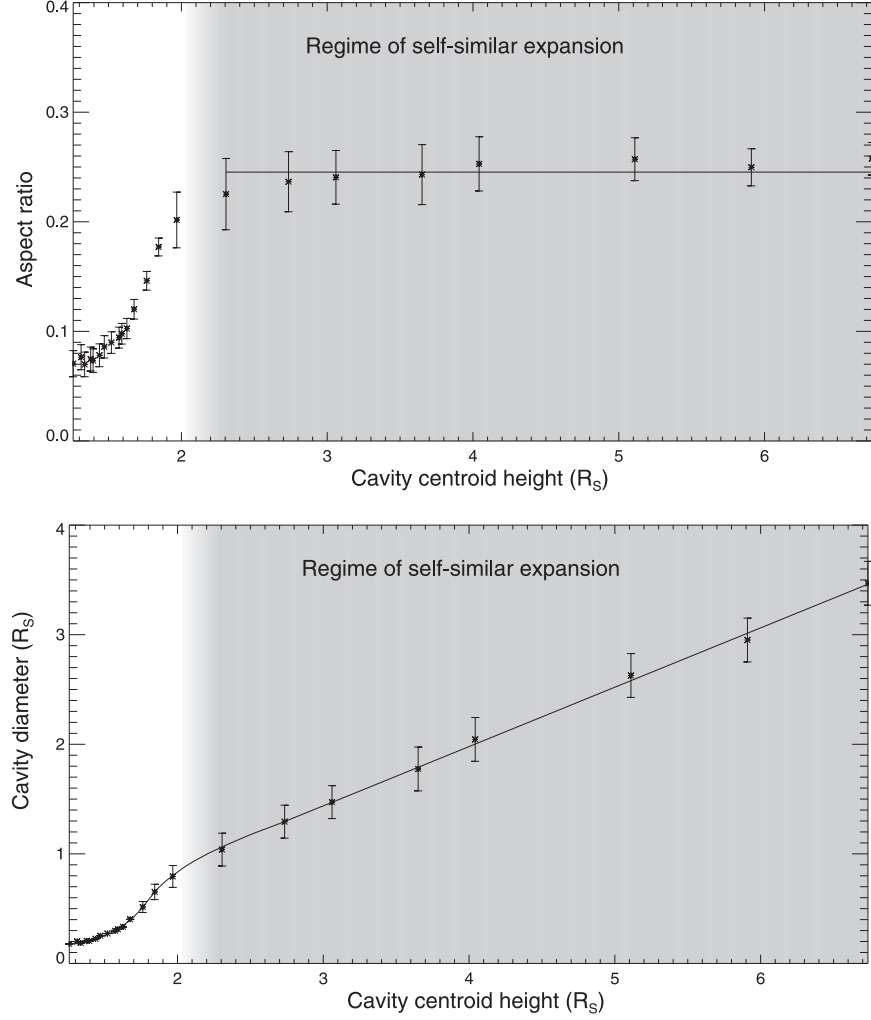


Figure 14. The evolution of the cavity width to centroid height aspect ratio (top panel). Evolution of the length along the semimajor axis of the cavity with respect to the cavity centroid height (bottom panel).

4.6. Eruption Mechanism of the Coronal Cavity in the Context of Torus Instability

In order to understand the pre-eruptive stability conditions for quiescent cavities and the triggering mechanisms for those structures to erupt, we have examined the role of the background magnetic field in the context of torus instability. In order to obtain information on the overlying magnetic field, we have used the Potential Field Source Surface (PFSS) extrapolation code (Schrijver & De Rosa 2003) available in SolarSoft packages. As the minimum time cadence of the available extrapolated fields from the PFSS model is 6 hr, we have used the extrapolations carried out within the minimum temporal window from the observing time of the cavity. For each of the four different days when the cavity was observed sequentially on the east limb, the POS of *STEREO A* and *STEREO B*, and the west limb, the decay index of the overlying magnetic field has been evaluated along the radial direction through the cavity centroid lying on the respective POS. In order to calculate the decay index, we have used the following formulation:

$$\text{decay index } [n] = -\frac{\partial \log(B_h)}{\partial \log(h)},$$

where h is the height above the solar photosphere and B_h is the horizontal component of the external magnetic field obtained from the PFSS extrapolations (Török & Kliem 2005).

The critical value (n_{critical}) of the decay index for the onset of torus instability is believed to be close to 1.5 (Kliem & Török 2006). However, depending on the typical range of current-channel thicknesses expected in the corona, n_{critical} can vary within a range between 1.2 and 1.5 (Démoulin & Aulanier 2010). From the observational studies on prominence eruptions, the value of n_{critical} (0.9 to 1.1) at the top of the prominence has been found to be less than that found in the MHD simulations (Filippov 2013; Zuccarello et al. 2014; McCauley et al. 2015). Addressing this discrepancy between the models and observations, Zuccarello et al. (2016) performed a set of MHD simulations and have shown that the value of n_{critical} computed at the flux rope's axis is 1.4 ± 0.1 , while at the height of the top of the prominence, this value is 1.1 ± 0.1 . These results suggest that the choice of location (filament top or cavity centroid) to evaluate the decay index is important for comparing the observational and theoretical values of n_{critical} . The temporal evolution of the altitude of the filament top and the cavity centroid, as presented in the current paper, allows us to address the above-mentioned issue observationally.

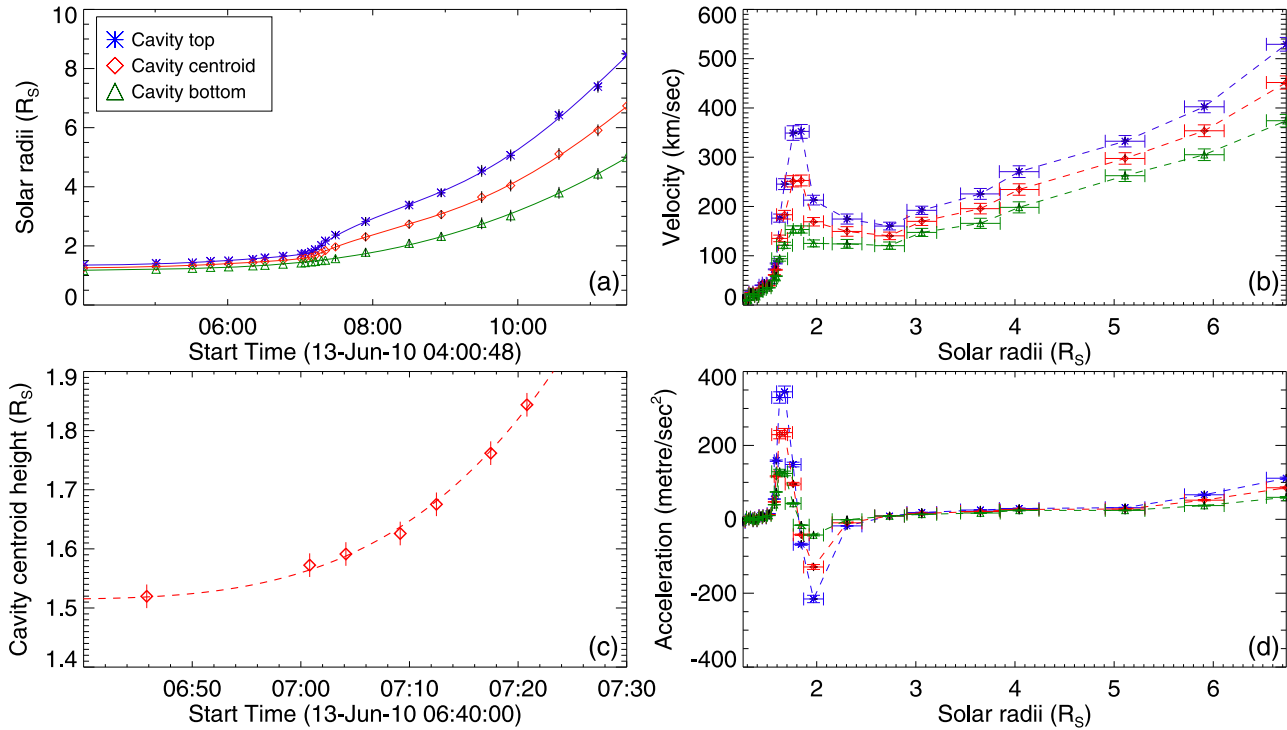


Figure 15. Height–time profiles for the cavity top, cavity centroid, and cavity bottom (a). Velocity profiles for the cavity top, cavity centroid, and cavity bottom (b). Polynomial fit to the cavity centroid height during the time interval 06:40 to 07:30 UT on 2010 June 13 (c). Acceleration profiles for the cavity top, cavity centroid, and cavity bottom (d).

Figure 16 shows the four decay-index profiles as calculated for the four different POS observations of the cavity along 90° E, 18° E, 20° W, and 90° W in Stonyhurst heliographic coordinates (Thompson 2006) on 2010 May 30, and June 4, 7, and 13, respectively. The overplotted black dashed and solid lines mark the decay-index values at the top of the filament and the cavity centroid respectively, which are listed in Table 2.

The decay-index values for the first three positions of the cavity during the observational period from 2010 May 4 to June 7 indicate that both the filament top and the cavity centroid reside well below the critical decay-index limit, while the cavity was in a stable condition (see Table 2). However, the decay-index value (1.3 ± 0.1) at the cavity centroid height reached the critical limit of 1.4 ± 0.1 for the onset of torus instability prior to the eruption on 2010 June 13. Noticeably, the altitude of the filament top also reached the decay-index value (1.2 ± 0.1), which resembles the “apparent” critical value (1.1 ± 0.1) of the decay index at the filament top as obtained from the simulation results of Zuccarello et al. (2016). Importantly, the good agreement between the observational (1.3 ± 0.1) and simulation (1.2 to 1.5) results for the critical decay-index value at the cavity centroid height suggests that the cavity centroid should be used as the preferred location to evaluate the decay-index value in order to reduce the discrepancy between the observational and theoretical critical limit for n_{critical} .

Furthermore, our results also suggest that the decay-index value at the cavity centroid height can be used as a good indicator for determining whether or not the cavity will result in an eruption.

Table 2
Temporal Evolution of the Decay Index

Observation Time yyyy/mm/dd hh:mm:ss	Decay Index at the Top of the Filament	Decay Index at the Cavity Centroid
2010 May 30 02:32:02	$0.75 \pm .07$	$0.80 \pm .06$
2010 Jun 4 21:25:30	$0.7 \pm .2$	$0.7 \pm .2$
2010 Jun 7 14:26:02	$0.7 \pm .1$	$0.8 \pm .1$
2010 Jun 13 04:00:00	$1.2 \pm .1$	$1.3 \pm .1$

5. Discussion and Conclusions

We have studied the morphological evolution of a two-week-long quiescent phase of coronal cavity by tracking the same portion of a large 3D structure associated with it. Combining the observations from SWAP, LASCO C2, and C3, we have also captured its evolution during the eruptive phase, which enables us to associate the erupting EUV cavity with its white-light counterpart as observed in the outer corona. The evolution of the cavity morphology at different stages of its quiescent and eruptive phases reveals the underlying eruption mechanism and the role of magnetic forces governing the cavity dynamics.

Observations from different vantage points during the quiescent phase reveal that the cavity morphology maintained a close to circular shape as it rotated across the solar disk. Eventually, the circular shape evolved into an elliptical one by the time the cavity reached the west solar limb, just prior to the eruption. It is important to note that the cavity centroid height slowly increased from 1.10 to $1.23 R_S$ in association with a slow expansion in the cavity size as it rotated from the east to west solar limb (see Table 1). Gibson & Fan (2006) demonstrated that

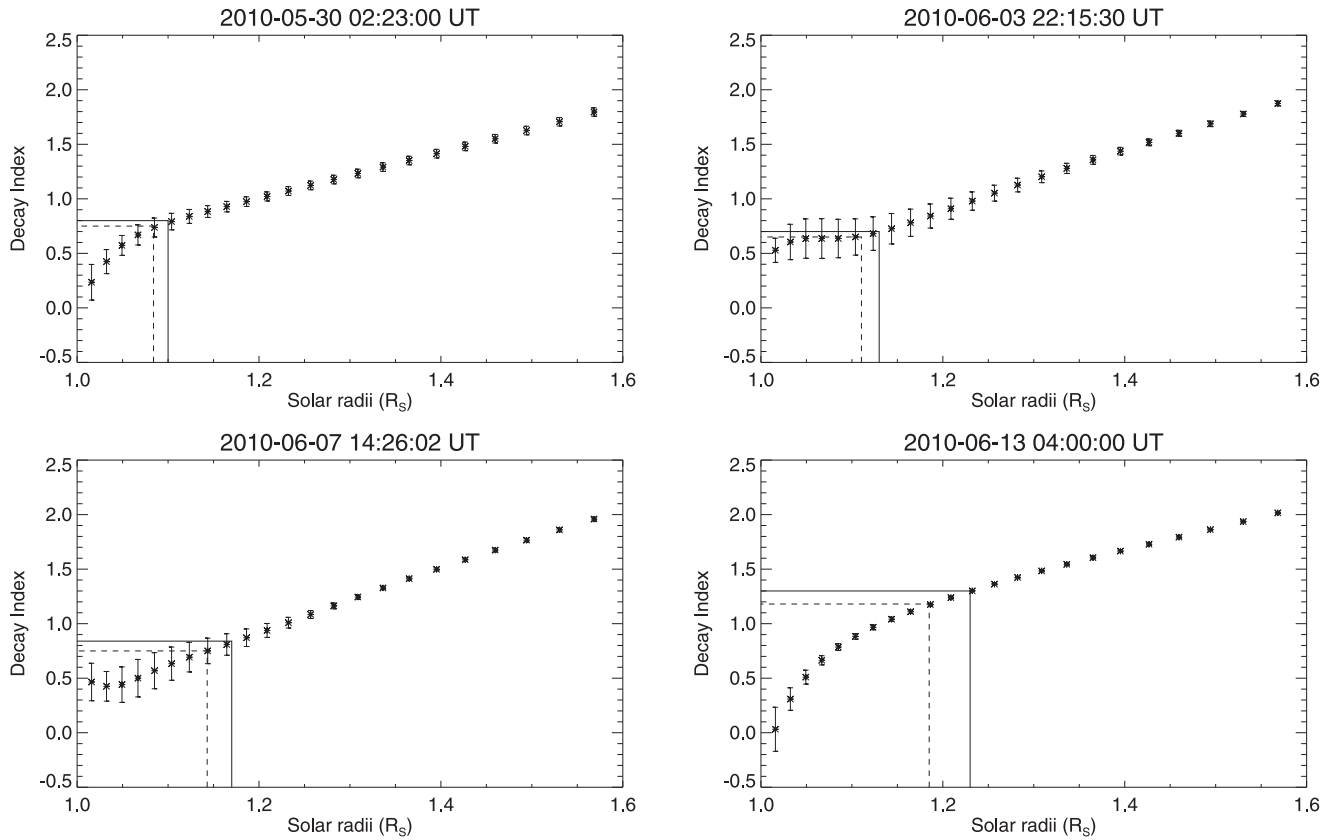


Figure 16. Decay-index profiles for the different phases of the quiescent cavity. The black solid and dashed lines mark the decay-index values at the cavity centroid and the top of the filament, respectively.

an expanding flux rope may achieve an equilibrium configuration when the forces causing the expansion are counterbalanced by the confining magnetic tension forces exerted by the overlying magnetic field. As the magnetic field strength drops off radially with height, it is expected that the flux rope equilibrium will be governed by a lateral confinement rather than a vertical one, resulting in an elliptical morphology of the flux rope cross section (Gibson 2015). Observations of the slowly rising and expanding cavity morphology presented in this work reveal that the cavity undergoes a series of stable equilibria during its quiescent phase. As the quiescent cavity expands and reaches higher heights in the corona, it becomes more elliptical, due to the excess magnetic pressure in the lateral direction exerted by the overlying magnetic field.

Interestingly, during the eruptive phase, the elliptical cavity morphology again transformed back into a close to circular shape when the cavity centroid height crossed $\approx 4 R_s$ in the FOV of LASCO C3. This implies that the confining magnetic tension forces fall off more rapidly with increasing radial height in comparison to the internal forces, causing the cavity expansion. Therefore, the domination of the internal expansion forces over the external magnetic tension force results in an isotropic expansion of the cavity which makes the cavity morphology close to circular in shape. This scenario is in agreement with the earlier findings of Chen et al. (2000), where it has been shown that the role of magnetic tension forces becomes less significant compared to the drag and hoop forces after the main acceleration phase of the CME, which tends to occur below 2–3 R_s (Chen & Krall 2003; Joshi & Srivastava 2011).

The slowly rising and expanding phase of the quiescent cavity (see Table 1) during its passage from the east to west solar limb holds intriguing clues to the underlying magneto-static equilibria of the cavity system. During this stage, the injection of helical poloidal flux through flows or flux emergence from the lower boundary may gradually increase the toroidal current of the associated flux rope, which results in a gradual build-up of Lorentz self-force in the cavity system (Chen et al. 2006). Therefore, the cavity centroid height showed a slow rise (Table 1), due to the gradual increase in the upward Lorentz self-force against the downward magnetic tension force exerted by the overlying magnetic field. Examining the decay-index profiles during the quiescent phase of the cavity, we have found that the decay-index value (< 1.0) at the cavity centroid height resided well below the critical value (1.2 to 1.5) for the onset of torus instability. This implies that although there was a slow build-up in the Lorentz self-force of the cavity system, it was not strong enough to overcome the downward magnetic tension forces, due to the strong overlying magnetic field strength. However, when the cavity appeared on the west solar limb, its centroid height attained a decay-index value ($1.3 \pm .01$) that belongs to the critical range (1.2 to 1.5) for the onset of a torus instability, and eventually it erupted from the west solar limb. Therefore, we conclude that the decay-index value at the cavity centroid height can be used as a good indicator to examine whether or not a cavity will lead to an eruption.

In what follows, we summarize the answers to the key questions (outlined in Section 1) that have been addressed in this study:

- (i) The slowly rising and expanding phases of the quiescent cavity hold important clues to its morphological evolution, which reveals that the cavity undergoes a sequence of quasi-static equilibria during its long-lived quiescent phase. As the slowly rising cavity reaches higher heights in the corona, its morphology transforms from a nearly circular to an elliptical shape, due to the excess magnetic pressure in the lateral direction exerted by the overlying magnetic field.
- (ii) Throughout the quiescent phase, the cavity centroid height resided well below the critical limit for the onset of torus instability. However, the cavity centroid reached the critical height for the onset of torus instability just prior to the eruption. This critical height ($1.23 R_S$) in the lower corona determines the initiation height of the associated CME.
- (iii) Evaluating the decay-index profiles at both the topmost part of the filament and the cavity centroid height, we conclude that the cavity centroid should be used as the preferred location to evaluate the decay-index value in order to reduce the discrepancy between the observational and theoretical critical limits for n_{critical} . Moreover, the decay-index value of the cavity centroid height can be used as a good indicator to determine whether or not the cavity will result in an eruption.
- (iv) Using the combined FOV of SWAP, and LASCO C2 and C3, we have shown how an EUV cavity evolved into a white-light cavity, as one of the three-part structure of a CME, while maintaining the same spatial relationship with the underlying prominence material.
- (v) The kinematic study of the cavity evolution successfully captures the two distinct phases of acceleration, where the impulsive acceleration phase was observed at $1.67 \pm 0.08 R_S$. The exponent value for the polynomial fit to the height–time profile of the erupting cavity reveals that the impulsive acceleration phase was most likely to be driven by the torus instability. However, during the residual acceleration phase, the Lorentz self-force was less dominant and the kinematic evolution became strongly dependent on the drag force.
- (vi) The significant nonradial motion observed in the SWAP FOV shows a strong deflection of the CME at lower coronal height ($\approx 1.3 R_S$). A deflection ($\approx 40^\circ$ toward the equator) of the CME trajectory from higher to lower latitudes indicates that the polar coronal hole has significant influence on the CME kinematics, deflecting the CME toward the heliospheric current sheet.
- (vii) Finding the critical height above which the CME undergoes self-similar expansion is one of the important results of this study. Interestingly, the critical height ($2.2 \pm 0.2 R_S$) below which the cavity exhibited non-self-similar expansion points to the spatial scale of magnetic field lines fundamentally changing from a closed to an open regime, as they open into the solar wind.

These findings can be statistically validated with a larger data set of events, which is beyond the scope of this current paper. In the future, we plan to carry out a statistical study on erupting cavities in order to get deeper insight into the CME initiation mechanism.

We thank the referee for helpful comments that improved the quality of this manuscript. R.S. and N.S. would like to

acknowledge the *PROBA2* Guest Investigator program grant received to carry out this work. The *PROBA2* Guest Investigator program grant and SWAP are projects of the Centre Spatial de Liege and the Royal Observatory of Belgium funded by the Belgian Federal Science Policy Office (BELSPO). E.D. acknowledges support from the Belgian Federal Science Policy Office (BELSPO) through the ESA-PRODEX programme, grant No. 4000120800. The authors also acknowledge the use of the data from *SDO/AIA* and *STEREO/EUVI*.

ORCID iDs

- Ranadeep Sarkar <https://orcid.org/0000-0001-6457-5207>
 Nandita Srivastava <https://orcid.org/0000-0002-0452-5838>
 Marilena Mierla <https://orcid.org/0000-0003-4105-7364>
 Matthew J West <https://orcid.org/0000-0002-0631-2393>
 Elke D’Huys <https://orcid.org/0000-0002-2914-2040>

References

- Bein, B. M., Berkebile-Stoiser, S., Veronig, A. M., Temmer, M., & Vršnak, B. 2012, *ApJ*, **755**, 44
 Brueckner, G. E., Howard, R. A., Koomen, M. J., et al. 1995, *SoPh*, **162**, 357
 Byrne, J. P., Maloney, S. A., McAteer, R. T. J., Refojo, J. M., & Gallagher, P. T. 2010, *NatCo*, **1**, 74
 Byrne, J. P., Morgan, H., Seaton, D. B., Bain, H. M., & Habbal, S. R. 2014, *SoPh*, **289**, 4545
 Chen, J., & Krall, J. 2003, *JGRA*, **108**, 1410
 Chen, J., Marqué, C., Vourlidas, A., Krall, J., & Schuck, P. W. 2006, *ApJ*, **649**, 452
 Chen, J., Santoro, R. A., Krall, J., et al. 2000, *ApJ*, **533**, 481
 Chen, P. F. 2011, *LRSP*, **8**, 1
 Cremades, H., Bothmer, V., & Tripathi, D. 2006, *AdSpR*, **38**, 461
 Daglis, I., Baker, D., Kappenman, J., Panasyuk, M., & Daly, E. 2004, *SpWea*, **2**, S02004
 Del Zanna, G., & Mason, H. E. 2018, *LRSP*, **15**, 5
 Démoulin, P., & Aulanier, G. 2010, *ApJ*, **718**, 1388
 Elmore, D. F., Burkepile, J. T., Darnell, J. A., Lecinski, A. R., & Stanger, A. L. 2003, *Proc. SPIE*, **4843**, 66
 Filippov, B. 2013, *ApJ*, **773**, 10
 Fisher, R. R., & Poland, A. I. 1981, *ApJ*, **246**, 1004
 Forland, B. C., Gibson, S. E., Dove, J. B., Rachmeler, L. A., & Fan, Y. 2013, *SoPh*, **288**, 603
 Gibson, S. 2015, in Coronal Cavities: Observations and Implications for the Magnetic Environment of Prominences, ed. J.-C. Vial & O. Engvold (Cham: Springer), 323
 Gibson, S. E., & Fan, Y. 2006, *JGRA*, **111**, A12103
 Gibson, S. E., Fludra, A., Bagenal, F., et al. 1999, *JGR*, **104**, 9691
 Gibson, S. E., Kucera, T. A., Rastawicki, D., et al. 2010, *ApJ*, **724**, 1133
 Gibson, S. E., Kucera, T. A., White, S. M., et al. 2016, *FrASS*, **3**, 8
 Gosling, J. T. 1993, *PhFB*, **5**, 2638
 Guennou, C., Rachmeler, L., Seaton, D., & Auchère, F. 2016, *FrASS*, **3**, 14
 Halain, J.-P., Berghmans, D., Seaton, D. B., et al. 2013, *SoPh*, **286**, 67
 Hoeksema, J. T. 1984, PhD thesis, Stanford Univ., CA
 Howard, R. A., Moses, J. D., Vourlidas, A., et al. 2008, *SSRv*, **136**, 67
 Howard, T. A., & DeForest, C. E. 2012, *ApJ*, **752**, 130
 Howard, T. A., DeForest, C. E., Schneck, U. G., & Alden, C. R. 2017, *ApJ*, **834**, 86
 Hundhausen, A. 1999, in The Many Faces of the Sun: A Summary of the Results From NASA’s Solar Maximum Mission, ed. K. T. Strong (New York: Springer), 143
 Illing, R. M. E., & Hundhausen, A. J. 1985, *JGR*, **90**, 275
 Inhester, B. 2015, arXiv:1512.00651
 Joshi, A. D., & Srivastava, N. 2011, *ApJ*, **739**, 8
 Kliem, B., & Török, T. 2006, *PhRvL*, **96**, 255002
 Lemen, J. R., Title, A. M., Akin, D. J., et al. 2012, *SoPh*, **275**, 17
 Liu, R., Alexander, D., & Gilbert, H. R. 2007, *ApJ*, **661**, 1260
 Low, B. C., & Hundhausen, J. R. 1995, *ApJ*, **443**, 818
 MacQueen, R. M., & Fisher, R. R. 1983, *SoPh*, **89**, 89
 Marićić, D., Vršnak, B., Stanger, A. L., & Veronig, A. 2004, *SoPh*, **225**, 337
 Martínez-Sykora, J., De Pontieu, B., Testa, P., & Hansteen, V. 2011, *ApJ*, **743**, 23

- McCauley, P. I., Su, Y. N., Schanche, N., et al. 2015, *SoPh*, **290**, 1703
- Mierla, M., Seaton, D. B., Berghmans, D., et al. 2013, *SoPh*, **286**, 241
- Morgan, H., Habbal, S. R., & Woo, R. 2006, *SoPh*, **236**, 263
- Panasenco, O., Martin, S., Joshi, A. D., & Srivastava, N. 2011, *JASTP*, **73**, 1129
- Rachmeler, L. A., Gibson, S. E., Dove, J. B., DeVore, C. R., & Fan, Y. 2013, *SoPh*, **288**, 617
- Régnier, S., Walsh, R. W., & Alexander, C. E. 2011, *A&A*, **533**, L1
- Santandrea, S., Gantois, K., Strauch, K., et al. 2013, *SoPh*, **286**, 5
- Schmahl, E. J. 1979, in IAU Coll. 44, Physics of Solar Prominences, ed. E. Jensen, P. Maltby, & F. Q. Orrall (Oslo: Inst. Teor. Astrophys.), 102
- Schrijver, C. J., & De Rosa, M. L. 2003, *SoPh*, **212**, 165
- Schrijver, C. J., Elmore, C., Kliem, B., Török, T., & Title, A. M. 2008, *ApJ*, **674**, 586
- Seaton, D. B., Berghmans, D., Nicula, B., et al. 2013, *SoPh*, **286**, 43
- Siscoe, G. 2000, *JASTP*, **62**, 1223
- Sterling, A. C., & Moore, R. L. 2004, *ApJ*, **602**, 1024
- Thompson, W. T. 2006, *A&A*, **449**, 791
- Török, T., & Kliem, B. 2005, *ApJL*, **630**, L97
- Vaiana, G. S., Krieger, A. S., & Timothy, A. F. 1973, *SoPh*, **32**, 81
- Vourlidas, A., & Howard, R. A. 2006, *ApJ*, **642**, 1216
- Vourlidas, A., Lynch, B. J., Howard, R. A., & Li, Y. 2013, *SoPh*, **284**, 179
- Vršnak, B., Ruždjak, D., Sudar, D., & Gopalswamy, N. 2004, *A&A*, **423**, 717
- Waldmeier, M. 1970, *SoPh*, **15**, 167
- Williams, D. R., Török, T., Démoulin, P., van Driel-Gesztelyi, L., & Kliem, B. 2005, *ApJL*, **628**, L163
- Wuelser, J.-P., Lemen, J. R., Tarbell, T. D., et al. 2004, *Proc. SPIE*, **5171**, 111
- Yurchyshyn, V. B. 2002, *ApJ*, **576**, 493
- Zuccarello, F. P., Aulanier, G., & Gilchrist, S. A. 2016, *ApJ*, **821**, L23
- Zuccarello, F. P., Seaton, D. B., Mierla, M., et al. 2014, *ApJ*, **785**, 88